Seasonality and Meridional Propagation of the MJO

MAN-LI C. WU, SIEGFRIED D. SCHUBERT, MAX J. SUAREZ, AND PHILIP J. PEGION*

Global Modeling and Assimilation Office, Earth–Sun Exploration Division, NASA Goddard Space Flight Center, Greenbelt, Maryland

DUANE E. WALISER

NASA Jet Propulsion Laboratory, Pasadena, California

(Manuscript received 14 March 2005, in final form 22 July 2005)

ABSTRACT

The Madden–Julian oscillation (MJO) is known to have a substantial impact on the variability of the Asian–Australian summer monsoons. An important, but not well understood, aspect of the MJO–monsoon connection is the meridional propagation of bands of enhanced or reduced precipitation that are especially pronounced during the northern summer. In this study, the nature of the seasonality of the MJO is examined, with a focus on the meridional propagation, using both observations and simulations with an atmospheric general circulation model (AGCM).

A key result is that the AGCM, when forced with idealized eastward propagating equatorial dipole heating anomalies, reproduces the salient features of the observed seasonality in the precipitation and wind fields associated with the MJO, including meridional propagation into the Indian and Australian summer monsoon regions. An analysis of the simulations and observations shows that the off-equatorial precipitation anomalies are initiated by surface frictional convergence/divergence associated with the Rossby wave response to the leading pole of the equatorial heating dipole. The off-equatorial precipitation anomalies develop further by interacting with the trailing pole of the equatorial dipole heating to produce a northwest–southeast (or southwest–northeast) oriented line of surface convergence/divergence that propagates to the east. Since the prescribed heating does not vary by season, the seasonal asymmetry in the response must be the result of the seasonal changes in the background state. In particular, the results suggest that seasonal changes in both the vertical wind shear and static stability play a role.

1. Introduction

The Madden–Julian oscillation (MJO: Madden and Julian 1972) is perhaps one of the best known and most studied atmospheric phenomena. As a result, progress has been made in our understanding of the basic mechanism of the MJO (e.g., Hendon and Salby 1994; Zhang et al. 2005, manuscript submitted to *Climate Dyn.*). Nevertheless, the pronounced seasonality of the MJO is still poorly understood. In particular, it is now well documented that the boreal winter MJO is predominately an eastward propagating phenomena, while the boreal summer MJO exhibits a more complex behavior, including northward propagation over the Indian and western Pacific Oceans (Lau and Chan 1986; Chen and Murakami 1988; Gadgil 1990; Ferranti et al. 1999; Annamalai et al. 1999) and westward propagation over the western North Pacific (Lau and Chan 1986; Wang and Xie 1997; Annamalai and Slingo 2001). In fact, the pronounced differences in the behavior of the MJO during boreal winter and summer have led some researchers to distinguish the summer MJO by renaming it the intraseasonal oscillation (ISO).

The meridional propagation of the MJO is of more than just scientific interest. It appears to be the primary mechanism by which the MJO impacts the Indian summer monsoon. The role of 30–50-day oscillations in the Indian monsoon was recognized in the early observational studies by Yasunari (1981) and Krishnamurti and Subrahmanyam (1982). They described a series of zonally oriented meridionally propagating troughs and ridges that seemed to form over the equatorial Indian

* Additional affiliation: Science Applications International Corporation, Beltsville, Maryland.

Corresponding author address: Man-Li C. Wu, NASA GSFC, Code 610.1, Greenbelt, MD 20771.
E-mail: man-li.c.wu@nasa.gov

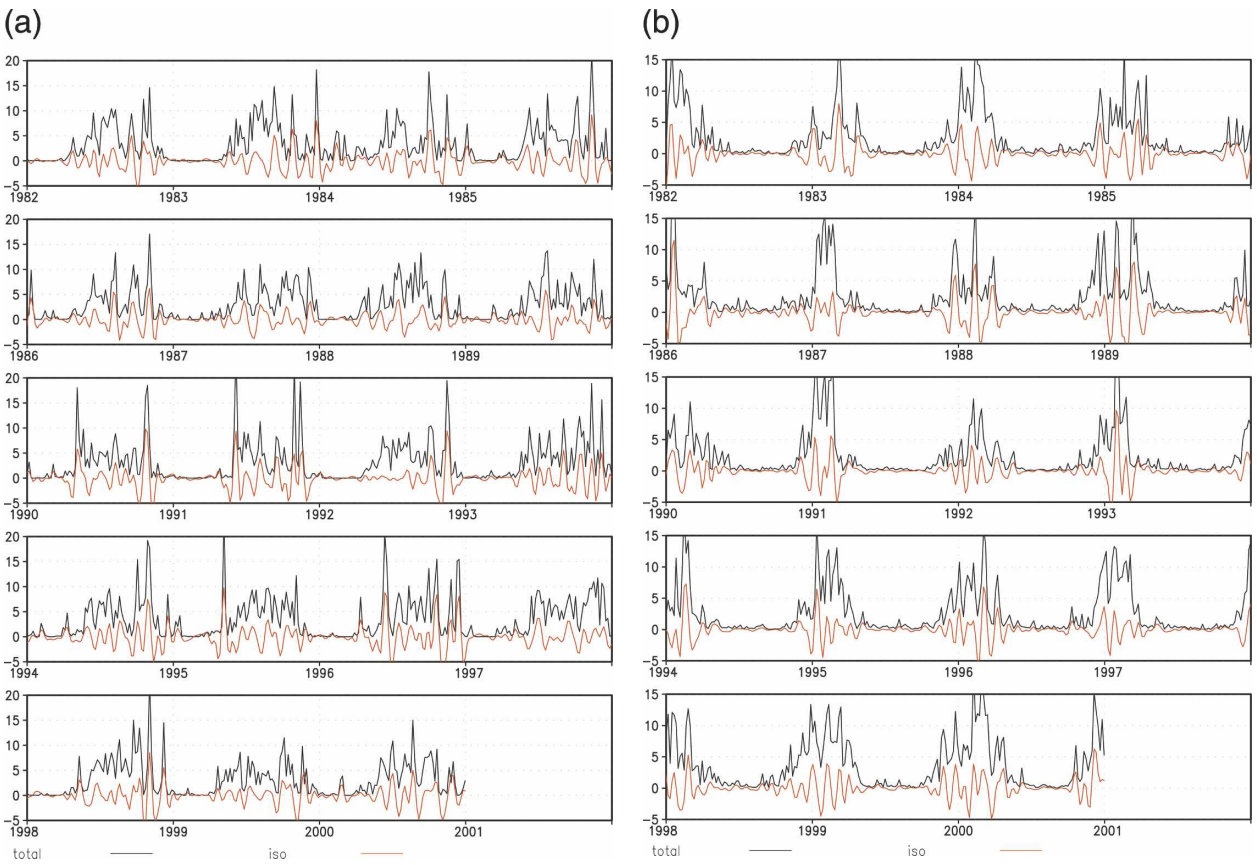

FIG. 1. (a) Mean GPCP precipitation (mm day^{-1}) averaged over central India between 10° and 15°N, 75° and 80°E and (b) over northern Australia between 20° and 10°S, 130° and 140°E. The black line is total precipitation, and the red line is the precipitation filtered to retain MJO/ISO time scales using a symmetric, four-pole, low-pass tangent Butterworth filter.

Ocean and dissipate near the Himalayas. This phenomenon was described in terms of transient Hadley cells that appeared to be associated with the active and inactive phases of the Indian monsoon. Lau and Chan (1986) showed further that the Indian monsoon onsetas well as mei-yu onset appear to be correlated with the 40–50-day oscillations. Wu et al. (1999) showed a strong contribution from the ISO to the northeastward progression and onset of the monsoon rains over India.

For austral summer, McBride (1983) analyzed satellite imagery for the winter International Monsoon Experiment and found that the sudden monsoon onset in late December is connected with the activation and break of large-scale spatially organized convection. Radok and Grant (1957) and Radok (1971) showed that the onset of the Southern Hemisphere monsoon is accompanied by a sudden shift southward of the Southern Hemisphere subtropical jet stream. More recent analyses of longer datasets suggest that meridional propagation of the MJO, while most pronounced in boreal summer, also occurs during austral summer, acting to modulate the strength of the Australian summer monsoon. Figures 1a and 1b show, for example, time series of area mean precipitation over the Indian subcontinent averaged between 10° and 15°N from, 75° to 80°E and over northern Australia averaged between 20°–10°S from 130° to 140°E, respectively. The results show that the variation of total precipitation over the Indian subcontinent and northern Australia is highly correlated with precipitation on the MJO time scale (the filter function for the MJO time scale is described in section 2d). In particular, the correlation coefficient for India is 0.69 (May through October) and for northern Australia it is 0.88 (November through April). Here we define the MJO as having time scales between 20 and 90 days. These time scales account for 48% (45%) of the total summer (winter) variance for the Indian subcontinent (Australia).

It thus appears that understanding and ultimately predicting intraseasonal monsoon variability rests largely on improving our understanding and simulation of the seasonality and, in particular, the meridional propagation of the MJO. Lau and Chan (1986) noted that the eastward propagation appears to occur during

all seasons and suggest that this is due to the presence of an intrinsic equatorial wave mode. They speculate further that meridional propagation arises primarily as a result of interactions of the oscillation with the monsoon circulation. Other studies show that the intrinsic equatorial wave noted above consists of an eastward propagating convectively coupled Kelvin–Rossby wave in which frictional wave conditional instability of the second kind (CISK) plays a key role (e.g., Wang and Rui 1990; Hendon and Salby 1994; Maloney and Hartmann 1998). The basic structure of these waves is consistent with the Gill model response to diabatic heating (Gill 1980), consisting of a Kelvin wave (KW) packet to the east of the heating and two Rossby wave (RW) packets to the west. The latter correspond at upper levels to a pair of anticyclonic (cyclonic) RW gyres that are symmetric with respect to the equator and trail the positive (negative) heating anomalies. This suggests the possibility that the seasonality of the MJO, and in particular the meridional propagation and off-equatorial behavior, may be determined by how the seasonally varying environmental conditions (the basic state and lower boundary conditions) impact the RW response.

Lau and Peng (1990) suggested that convective feedback between the monsoon flow and the equatorial 30–50-day oscillation could trigger westward propagating baroclinic modes (unstable RWs under the influence of vertically sheared flow) over the summer monsoon region. The disturbances are linked to changes in the local Hadley circulation and are associated with enhanced convection immediately poleward of the region of maximum westerly flow over the monsoon region and a concomitant reduced convection over the equatorial region, consistent with the inverse relationship between the intertropical convergence zone (ITCZ) and monsoon precipitation found over India. The model results of Wang and Xie (1997) also show that the character of the ISO is strongly influenced by the background circulation and the low-level moisture distribution (determined in part by the underlying sea surface temperature). They associate the northward propagation of convection with the eastward movement of a northwest tilted packet of RW emanating from the equatorial convection. Kemball-Cook and Wang (2001) show observational evidence for an important role of RWs forced by equatorial convection in the northward propagation of convection over both the Indian and western Pacific Oceans. Lawrence and Webster (2002) show observational evidence for a strong link between equatorial eastward and northward propagation of convection on ISO (25–80 day) time scales over the south Asian summer monsoon region. They interpret the results in terms of a propagating equatorial mode where the northward-moving convection is forced by surface frictional convergence into the low pressure center of the Rossby cell excited by the equatorial convection. They note that a similar convergence pattern occurs for the northern winter ISO, but it does not generate poleward movement due to the relatively cooler winter SSTs.

In this study we use both observations and model simulations to address further the causes of the seasonality of the MJO. The focus is on the MJO's north–south asymmetries and meridional propagation and its links to intraseasonal variability of the Asian and Australian summer monsoons. We carry out a number of idealized atmospheric general circulation model (AGCM) experiments designed to further address the basic mechanism of meridional propagation proposed by Lawrence and Webster (2002). Specifically, our goal is to better understand and quantify the link between eastward and northward propagation and how that link varies with season. In our baseline AGCM experiments, the atmosphere is forced with an idealized "MJO like" heating distribution that is centered on the equator and propagates to the east with a period of 40 days. Since the specified heating does not vary with the seasons, any seasonal variations in the response to the heating (e.g., meridional propagation) must occur as a result of changes in the background state and/or lower boundary conditions. Further experiments are done to isolate the role of the annual cycle in SSTs.

Section 2 describes the observations, the AGCM, the design of the experiments, and the analysis methods. Section 3 describes the results of the idealized heating experiments, while section 4 examines the seasonal changes in the background state. The conclusions are given in section 5.

2. Methods and data

a. Observations

We use a number of observational quantities including precipitation, surface (10 m) winds, 100- and 200-hPa winds, and streamfunction. The precipitation product is from the Global Precipitation Climatology Project (GPCP). The data consist of 5-day averaged (pentad) values available beginning in January 1979 (Xie and Arkin 1997). The pentad data were produced by merging several kinds of precipitation data, including gauge observations, estimates inferred from infrared radiation measurements, and estimates based on the Special Sensor Microwave Imager (SSM/I) satellite observations. The winds at 10 m are based on SSM/I wind speed observations and include a derived wind direction as discussed in Atlas et al. (1996) and Atlas et

al. (2001). The wind data covers the period from 1988 through 1998. The streamfunction and winds at 100 and 200 hPa are based on ECMWF Re-Analysis (Gibson et al. 1996). We note that in Fig. 1 we use the precipitation data for the period 1982–2000. In all other figures we use the data for the period from 1988 to 1998 to match the time period of the surface wind data.

b. Model description

Our experiments are done with version 1 of the National Aeronautics and Space Administration (NASA) Seasonal–Interannual Prediction Project (NSIPP-1) AGCM. This model is part of the NSIPP coupled atmosphere land–ocean model; however, for these experiments it is run uncoupled from the ocean. NSIPP-1 is a gridpoint model using a fourth-order dynamical core with explicit leapfrog time differencing. The dynamical core is described in Suarez and Takacs (1995). The vertical coordinate is a standard sigma coordinate and the vertical differencing follows Arakawa and Suarez (1983). The experiments were run at a horizontal resolution of 2° latitude and 2.5° longitude. There are 34 levels in the vertical with higher resolution in the lower 2 km of the atmosphere (<200 m). The boundary layer scheme is a simple K-scheme, which calculates turbulent diffusivities for heat and momentum based on Monin–Obukhov similarity theory (Louis et al. 1982). Turbulent diffusivities are determined as a function of roughness length, the von Kármán constant, and a bulk boundary layer Richardson number. Vertical mixing of tracers is accomplished using the diffusivity for heat.

The model uses the relaxed Arakawa–Schubert (RAS) scheme to parameterize convection (Moorthi and Suarez 1992). RAS uses a sequence of simple linearly entraining plumes (clouds types) that originate at the lowest sigma level and detrain at specific model levels. The initial cloud-base mass flux for each cloud type is determined from a convective available potential energy closure (Arakawa and Schubert 1972). The RAS scheme effectively acts as a parameterization of both deep and shallow convection in our model. Bacmeister and Suarez (2002) show that the model produces a reasonable simulation of the thermodynamic structure of the lower troposphere. The parameterization of solar and infrared radiative heating used in the model is described in Chou and Suarez (1994, 1999). The solar heating includes absorption of O_3, CO_2, water vapor, O_2, and clouds as well a gaseous and aerosol scattering.

The climate of the NSIPP-1 model and further details of its formulation are described in Bacmeister et al. (2000). Other aspects of the model's climate and variability are described in Pegion et al. (2000), Schubert et al. (2002), and Waliser et al. (2003). Of particular importance for this study is that the model has only a very weak signature of the MJO: this is especially true for the precipitation-related fields (Waliser et al. 2003). While this is clearly a deficiency of the model, it is to our advantage in this study since it allows us to more easily isolate the model's response to an imposed subseasonal MJO-like heating anomaly (see below).

The extent to which the lack of an MJO affects other aspects of the model behavior is unclear though, as we shall see, the imposition of idealized MJO heating anomalies does seem to produce some improvements in the model climatology.

c. The AGCM experiments

The experiments consist of a number of different model runs. A 20-yr control run was made with a repeating annual cycle of climatological monthly SSTs. The SST climatology is based on the years 1930–98 (Rayner et al. 2003).

Our primary set of experiments consists of a 10-member ensemble of 1-yr runs with specified idealized heating anomalies designed to simulate the eastward propagating equatorial heating associated with the MJO (Park et al. 1995 and Fig. 2). The sinusoidal heating and cooling anomalies are imposed on the SST climatology of the control run, are symmetric with respect to the equator, and propagate to the east with a period of 40 days. A Gaussian envelope damps the propagating anomalies to zero west of about 30°E and east of about 150°W. The vertical distribution is such that the maximum heating (1.5°C day^{-1}) occurs at approximately 500 hPa. The 10 ensemble members are forced with the same prescribed heating for 12 months starting on 1 May, but differ in initial conditions, which are taken from 10 different 1 May restarts from the control run.

d. Analysis methods

To evaluate the temporal and spatial evolution of circulation and convection patterns associated with the MJO/ISO, we form composites based on an index consisting of area-averaged precipitation at selected equatorial base regions. Our base region typically extends from 4°S to 4°N and covers 30° of longitude. Values are included in the composite if the value of the index exceeds one standard deviation. In addition to these (lag 0) composites, we also include composite values at times immediately before and after the time of the local maximum in the index. We note that a similar analysis approach employing regression and/or correlations with a base index has been applied successfully in a

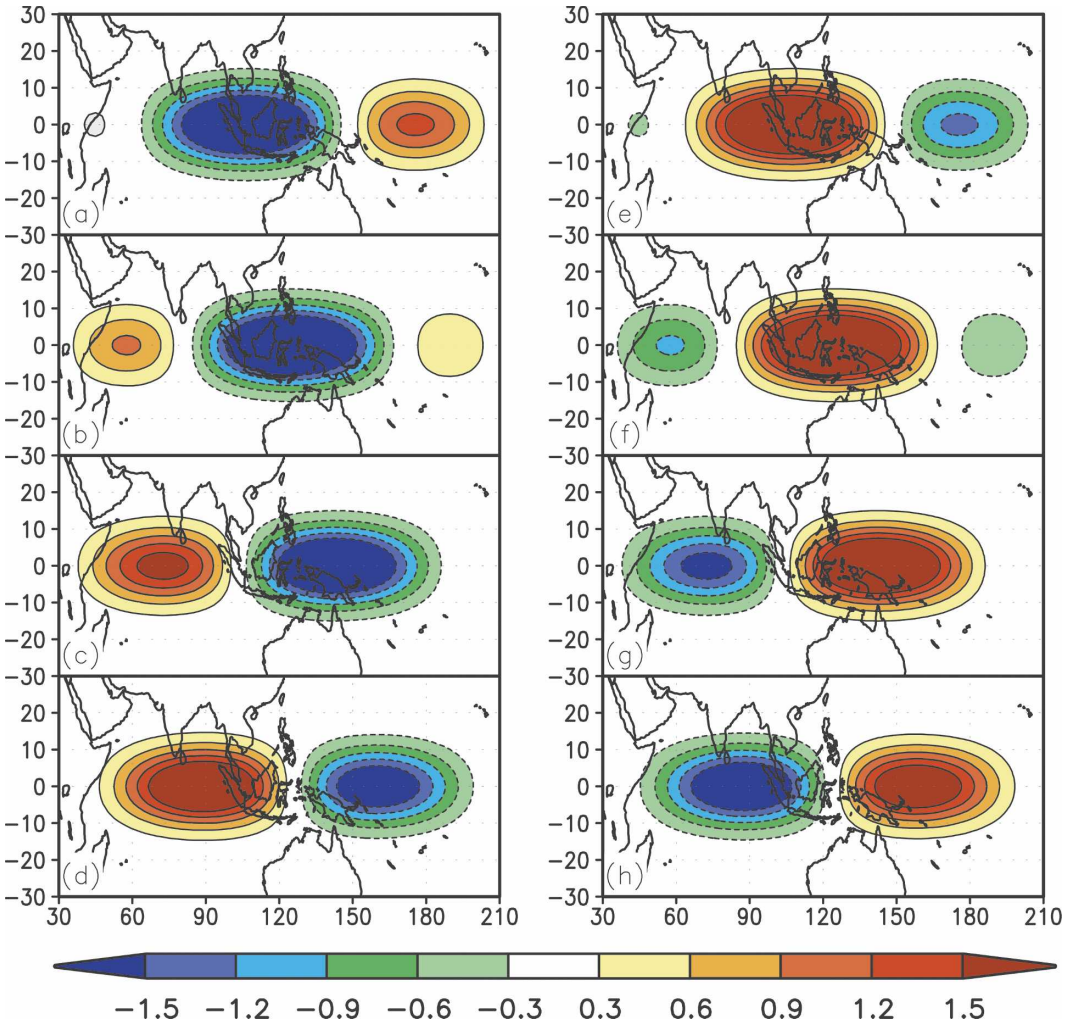

FIG. 2. The idealized MJO heating shown here at 500 mb for 5-day averages. The heating is symmetric with respect to the equator and propagates to the east with a period of 40 days. A Gaussian envelope damps the propagating anomalies to zero west of about 30°E and east of about 150°W. The vertical distribution is such that the maximum heating (1.5°C day^{-1}) occurs at approximately 500 hPa.

number of other studies of tropical heating variability (e.g., Kiladis and Weickmann 1992; Lawrence and Webster 2002).

All of the observational anomalies have a 20–90-day filter applied. The filter is a symmetric, four-pole, low-pass, tangent Butterworth filter described in Oppenheim and Schafer (1975). The filter is applied twice, first retaining time scales longer than 20 days and then retaining time scales longer than 90 days. The bandpass data are obtained by subtracting the two filtered datasets.

We have carried out a limited sensitivity study and have not found a strong sensitivity to the exact definition of either the MJO time scales or the region (the results are qualitatively similar). We chose the region to be large enough to encompass most of the winter and summer MJO variance. We chose the MJO time scales to encompass most definitions but to still exclude weather and seasonal and larger time scales.

For the observations, the base time series is extracted from the 20–90-day period filtered pentad precipitation data. The base time series is then used to composite the filtered time series at various time lags and at all other grid points as described above. The time lag is from −20 to +20 days. This method assumes that the relationship between precipitation and the circulation is nearly linear and that linear dynamics can describe much of the atmospheric response to tropical heating (Webster 1972; Gill 1980; Sardshmukh and Hoskins 1988). The same compositing procedure is applied to

the AGCM simulations, though in this case no filter is applied to the data (the regularity of the idealized forcing makes time filtering unnecessary). The model anomalies are constructed by subtracting the idealized forcing simulation from the control.

3. The idealized heating experiments

In the following subsections we present the results from the various model simulations and compare them with the observations. Subsection 3a shows the model climatology and some initial results from the idealized heating runs, including the impact of the imposed heating on the model climatology. This is followed by a focus (in sections 3b and 3c) on the boreal summer and winter seasons.

a. Model climatology and response to heating

Before examining the time-varying response to the heating, we take a brief look at the climatology of the control run. The top four panels of Fig. 3 show the average summer and winter precipitation from the observations and control simulation. While the model captures the basic seasonal variation of the precipitation and winds, the simulation tends to overestimate the precipitation amounts. There is a tendency to extend the high precipitation amounts too far to the north of the Pacific warm pool during boreal summer. There is also too little boreal summer precipitation over the eastern equatorial Indian Ocean. The model does a good job of simulating the seasonal changes in the surface winds.

The impact of the time-varying heating on the model climatology is shown in the two panels at the bottom of Fig. 3 in terms of the mean precipitation and surface wind differences between the idealized heating and control runs. Overall, the differences are small, except over the Maritime Continent and equatorial warm-pool regions. An examination of the surface evaporation and wind speed for these simulations (not shown) shows large wind speed variations and surface latent heat flux variations generated by the strong idealized heating over these regions. The generally small differences are the result of the cancellation that occurs when averaging over opposite phases of the imposed MJO heating.

Figure 3 also suggests that the imposed heating improves model performance somewhat by redistributing precipitation patterns over the summer and winter monsoon regions. We see, in particular, that during summer precipitation over the Maritime Continent, the Bay of Bengal, and east of the South China Sea is reduced, while precipitation over northern Sumatra and adjacent regions and over the southeastern South China Sea is enhanced. During winter, precipitation is suppressed over the eastern Indian Ocean, Sumatra, and the eastern South China Sea. While the differences are small, they nevertheless suggest that there is some rectification of the sinusoidal MJO signal that contributes to the climatology of these regions.

We next show the time-varying response of the model to the idealized heating averaged over all seasons. The total diabatic heating and precipitation anomalies are computed as the composite difference between the idealized heating simulations averaged over the 90 MJO cycles (ten cases times nine 40-day cycles per year) and the average of the control simulation (see sections 2c and 2d). The panels on the left side of Fig. 4 show the time evolution of the response in the total equatorial diabatic heating and precipitation anomalies. We note that the eight phases of the imposed heating (Fig. 2) correspond to the phases as shown in Figs. 4 and 5. We see that the total diabatic heating response and surface precipitation lags somewhat behind (to the west of) the imposed heating, with the strongest response occurring between about 120° and 160°E. In the vertical, the diabatict heating response maximizes at about 400 mb, slightly higher than the maximum of the imposed heating. The cross section at 70°E (right panels of Fig. 4) shows that the main positive diabatic heating anomaly in the Tropics at day 15 (near 400 mb) is associated with a downward extension (below 600 mb) of the heating anomalies on either side of the equator. The heating anomalies show considerable symmetry with respect to the equator. Over the course of 20 days the off-equatorial positive anomalies move poleward such that at day 35 the two heating anomalies have moved poleward of 10°, while the equatorial anomaly has changed sign.

Our focus in the following sections is on the seasonality of the model's response to the heating. Figure 5 shows, for example, the same north–south heating cross sections shown in Fig. 4, but in this case they are shown separately for boreal summer and winter. There is clearly strong asymmetry with respect to the equator during boreal summer, while the response is considerably more symmetric during boreal winter. In particular, the heating that develops north of the equator during boreal summer eventually dominates the response so that after day 25 the heating is largely confined to the northern latitudes (maximum at about 12°N). This occurs in a region of strong easterly shear, surface westerlies, and surface temperatures that exceed 28°C. The boreal winter response has a much stronger equatorial component with a tendency for the off-equatorial heat-

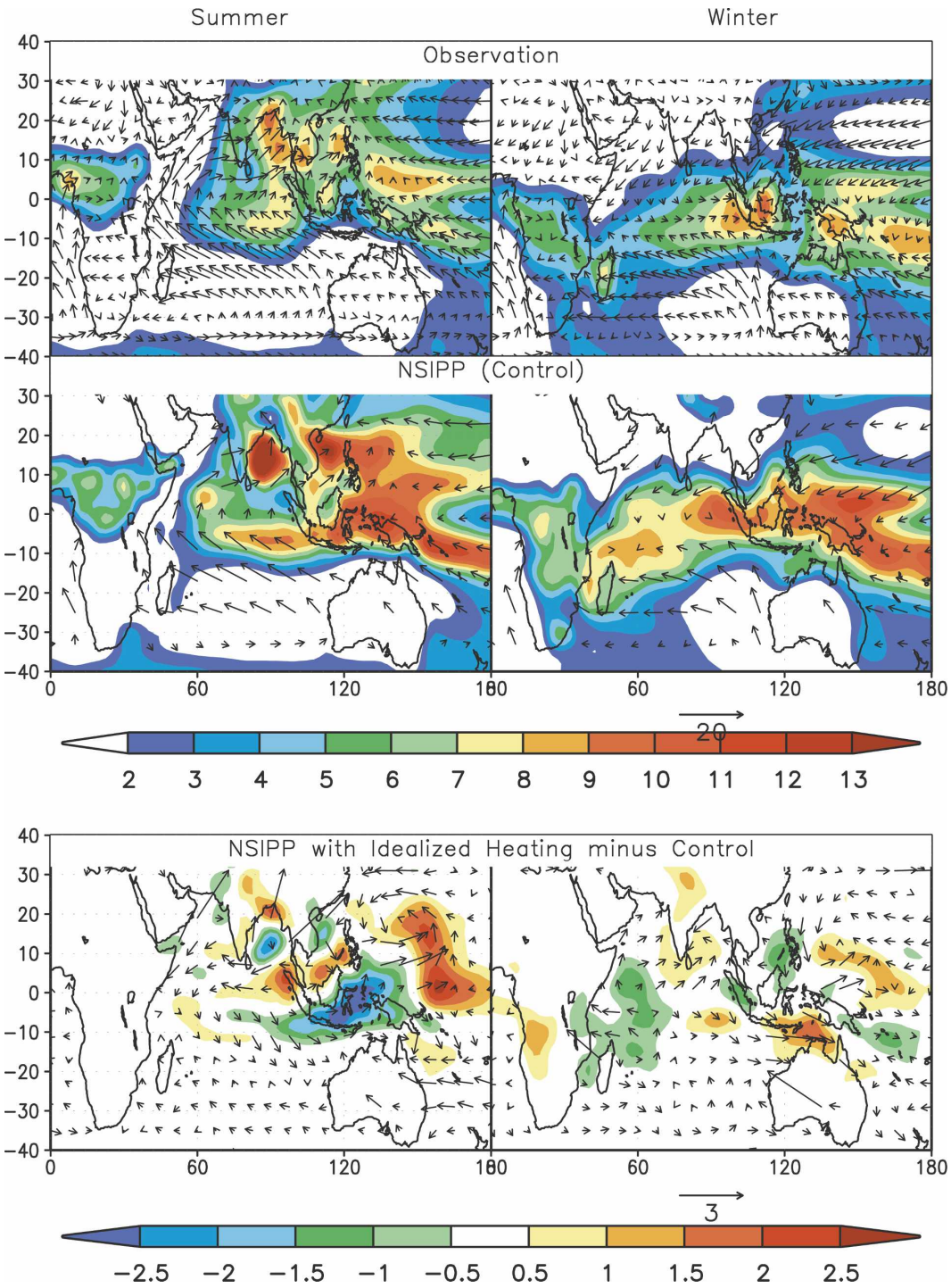

FIG. 3. The top four panels show the summer and winter mean precipitation (mm day^{-1}) and wind (m s^{-1}) from observations and model simulations. The bottom two panels are precipitation (mm day^{-1}) and surface wind differences (m s^{-1}) between the idealized heating simulation and control simulation.

ing anomaly to be larger in the Southern Hemisphere (SH) during strong positive equatorial heating, while it is larger in the Northern Hemisphere (NH) during periods with strong negative equatorial heating (we note a similar tendency for this to occur during boreal summer; see left panels of Fig. 5). In the following sections we look at the seasonality of the response in more detail.

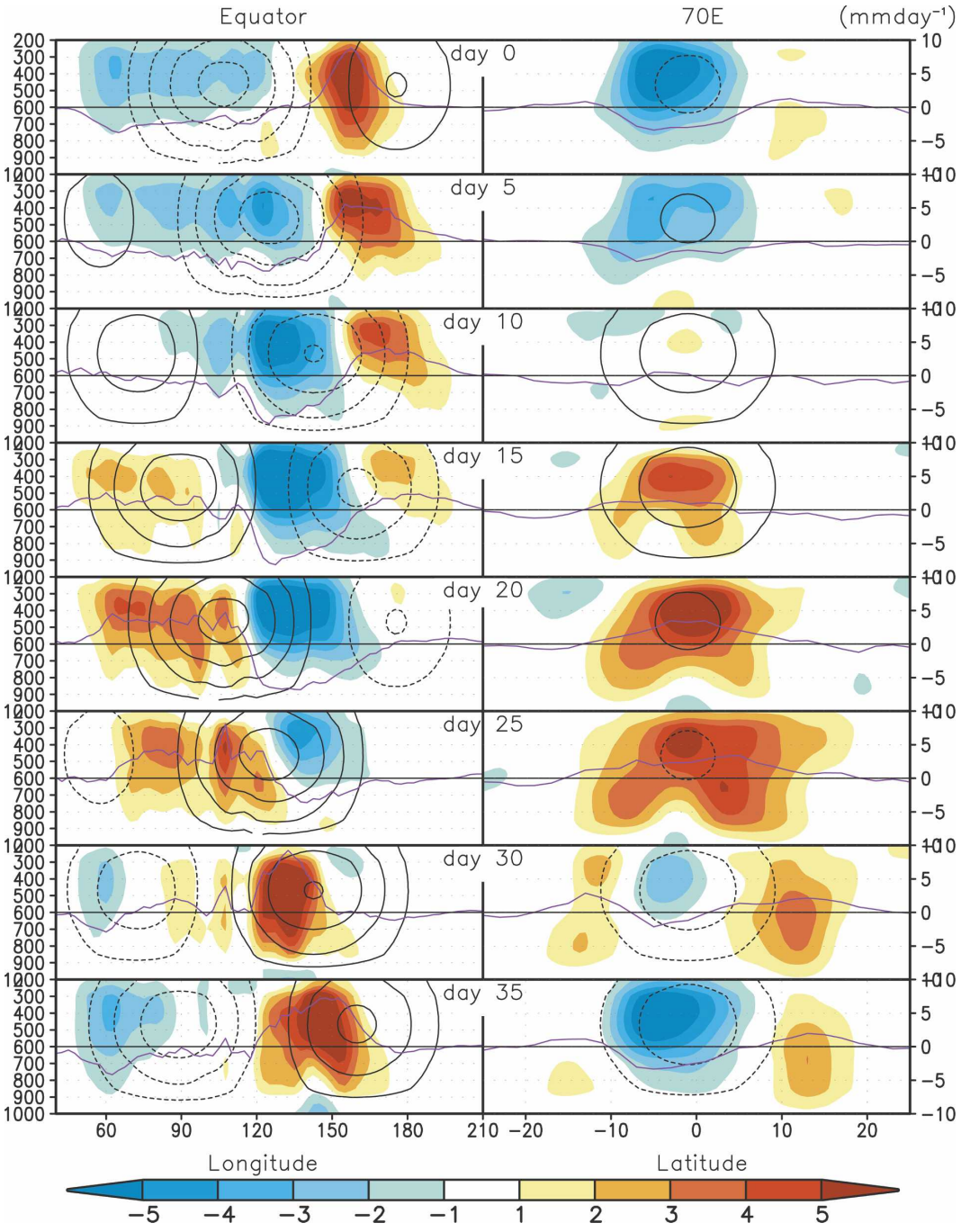

FIG. 4. The total diabatic heating (°C day^{-1}) and precipitation differences (mm day^{-1}) between the idealized heating simulations and control simulation. The differences are based on the averages of the 90 MJO cycles. The total diabatic heating differences are color shaded. The contoured field is the idealized heating (contour interval is 0.3°C, and negative values are shaded). The purple solid lines indicate the precipitation (right-hand axis). (left) Longitude–height cross sections at the equator and (right) latitude–height cross sections at 70°E.

b. Boreal summer (May–October)

Our method for compositing the model simulations and observations is described in section 2d. Our focus in this section is on describing the spatial structure and evolution of precipitation and circulation that is associated with subseasonal variations of the precipitation at or near the equator.

Figure 6 compares the evolution of the precipitation, surface winds, and upper-level streamfunction

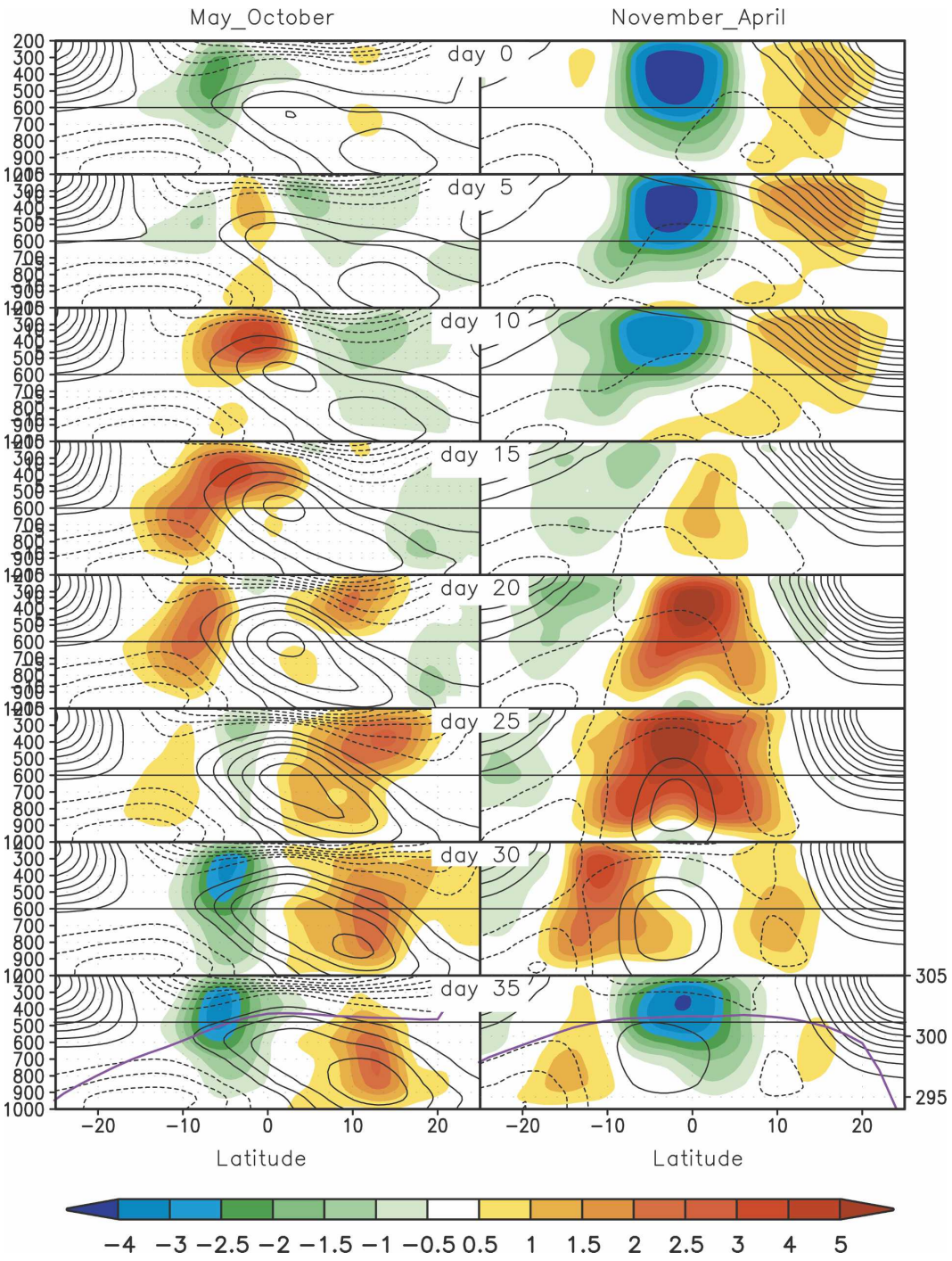

FIG. 5. Total diabatic heating differences (°C day^{-1}, shaded) and zonal winds (m s^{-1}, contour) at 70°E for summer and winter. The differences are based on the averages of approximately 45 warm or cold season MJO cycles. The purple line is SST and the horizontal lines are SST at 28°C.

(100 hPa) from the model and observations. We note that day 0 in Fig. 6 corresponds to the time when the idealized heating is at a phase halfway between those shown in Figs. 2d and 2e. Generally, the model reproduces the patterns of the observed precipitation and wind anomalies, though the precipitation and wind anomalies are about a factor of 2 too large. The simulated precipitation anomalies are especially unrealistic

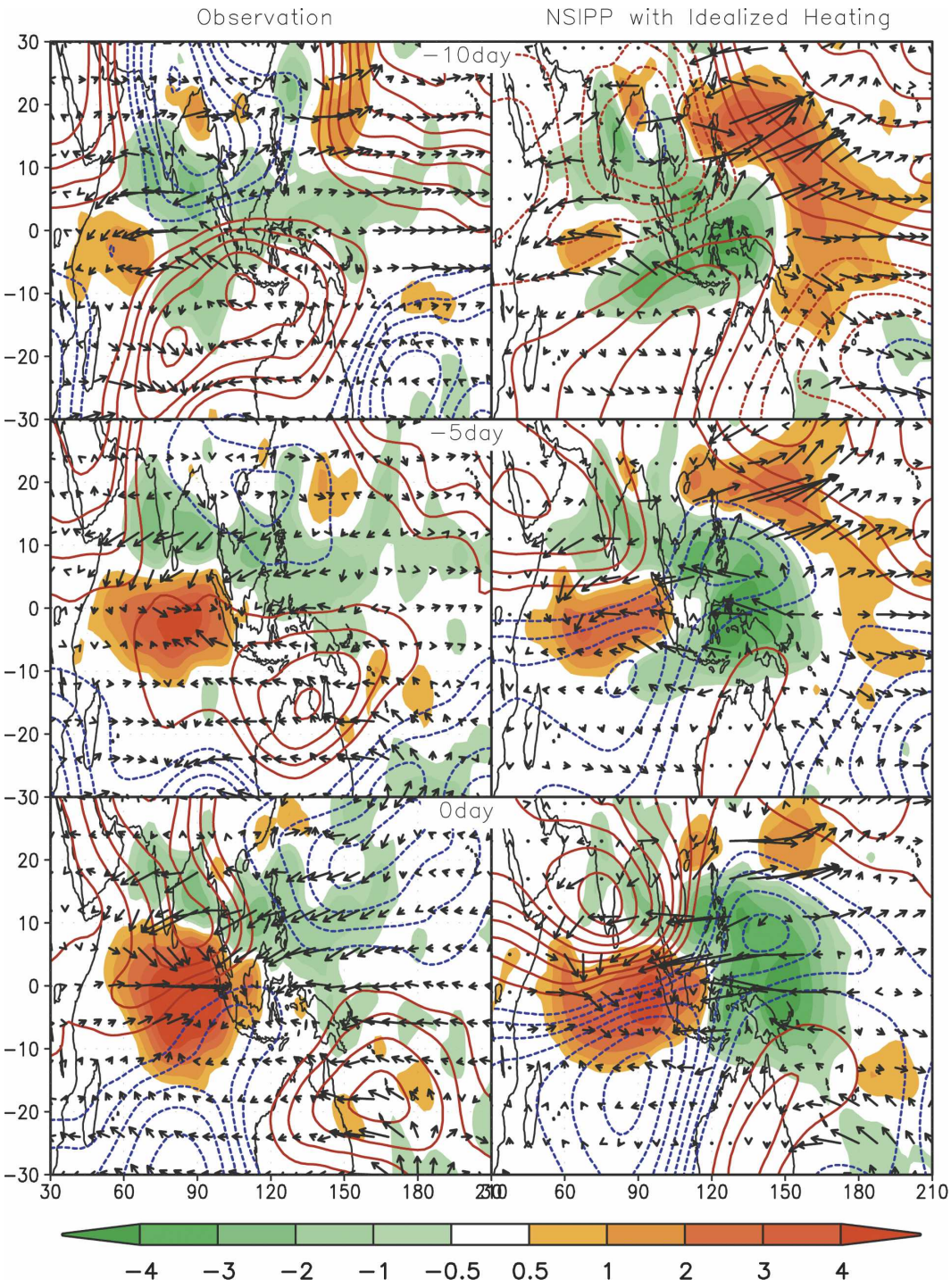

FIG. 6. Composite precipitation (mm day^{-1}) and surface wind (m s^{-1}) anomaly lags ranging from −15 to 0 days. (left) Observations and (right) observations based on NSIPP-1 AGCM simulations with idealized heating.

over the warm pool region where they are both too large and spatially too coherent compared with the observations. Nevertheless, both simulation and observations show very similar eastward propagation of the positive and negative precipitation anomalies. Both also show clear evidence of a northward migration of bands of enhanced or reduced precipitation that cross the Indian subcontinent. In particular, the enhanced

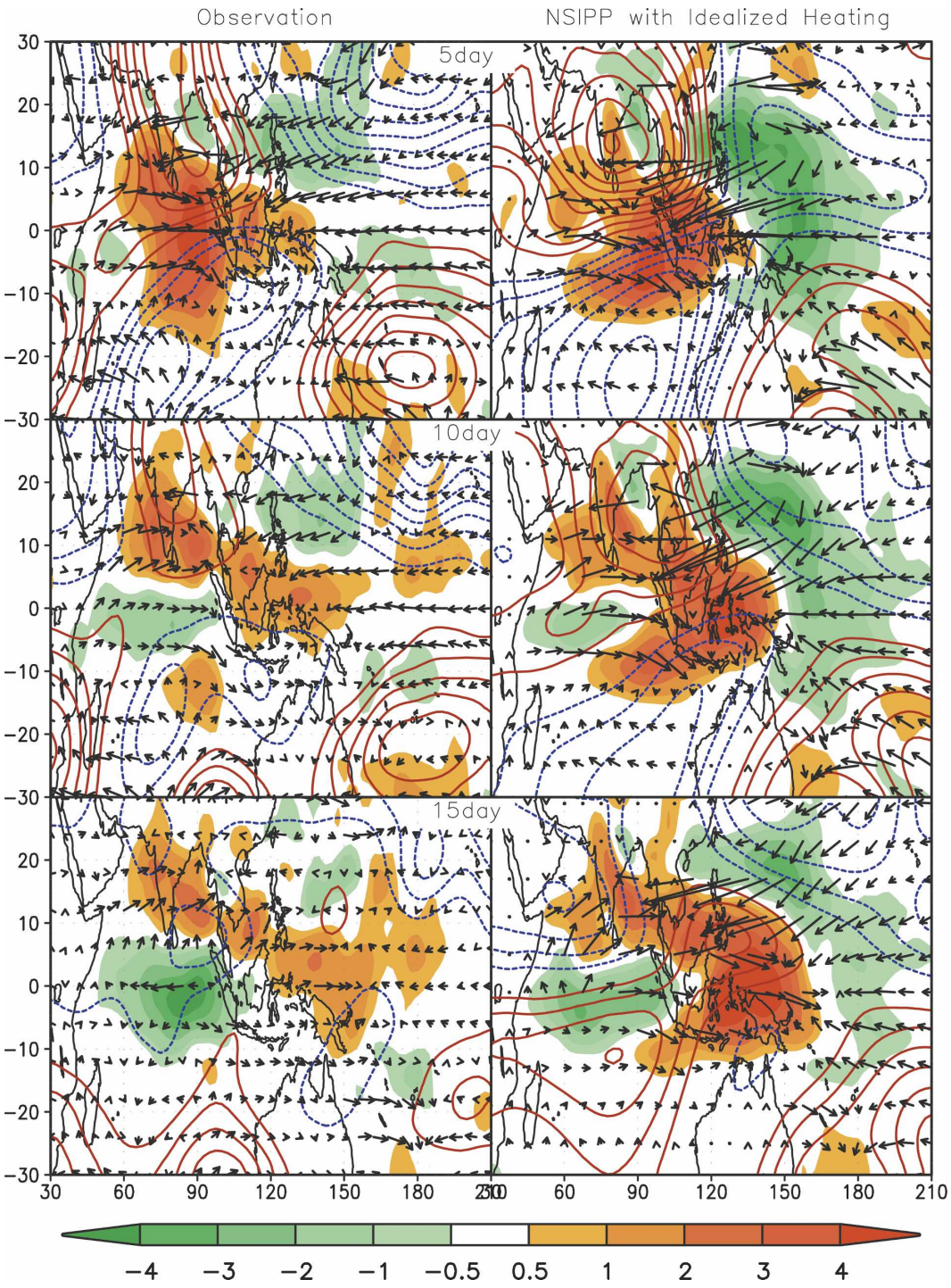

FIG. 6. (*Continued*)

precipitation that occurs over India at day 15 appears to be the result of a split in the equatorial heating as it passes just south of the subcontinent at day 5. Associated with the split there is also evidence for southward migration of positive precipitation anomalies beginning at day 5, though that largely disappears by day 15. Similarly, the band of reduced precipitation that occurs over India at day −5 appears to be the result of a split in the negative precipitation anomaly between days −15 and −10.

The evolution of the off-equatorial anomalies de-

scribed above can be divided into two stages. The initial development is largely symmetric with respect to the equator. A split in the equatorial precipitation anomalies [between days −15 (not shown) and −10 for the negative anomaly and between days 0 and +5 for the positive anomaly] is apparently associated with the Rossby wave responses to the equatorial anomalies (pair of anticyclonic vortices straddling the equator at −10 days and cyclonic anomalies at +5 days).

In the next stage the development is largely asymmetric, favoring the environment of the summer hemisphere. Focusing on the evolution over the Indian monsoon region after day −10, we see that the north–south split (and resulting divergence) in the surface easterly anomalies, which was initiated by the Rossby wave anticyclone, expands across the Arabian Sea, India, and Bay of Bengal (Fig. 6). This occurs as a result of the northeasterlies that develop to the south, apparently as a response to the positive precipitation anomalies that move into and grow over the equatorial Indian Ocean. The northeasterlies (and associated reduced precipitation) eventually extend from the northern Arabian Sea southeastward across India into the Bay of Bengal and, together with the equatorial negative precipitation anomaly that at day 0 has moved over the Pacific warm-pool region, defines a northwest-to-southeast band of reduced precipitation. In contrast, in the winter hemisphere the off-equatorial negative precipitation anomalies fail to develop much beyond the initial split of the equatorial precipitation anomaly at day −10 (Fig. 6). The anomalies fail to develop despite the existence between days −5 and −10 of surface convergence (not shown) associated with the Southern Hemisphere Rossby wave anticyclone. The reasons for this are discussed in section 4.

An analogous development occurs for the positive precipitation anomalies after day +5 (Fig. 6). In this case, the cyclonic circulation anomalies, together with southwesterlies that develop to the south in response to the developing negative precipitation anomalies over the equatorial Indian Ocean, produce a northwest to southeast oriented band of enhanced precipitation. After the initial symmetric development tied to the Rossby wave response, the subsequent development (after day 5) again favors the summer hemisphere.

The upper-level streamfunction in the Fig. 6 shows that both observations and simulations have a quadrapole structure with a coherent eastward movement tied to the precipitation/heating anomalies. The structure is coherent, with westerly wind anomalies just to the east of the heating and easterlies to the east. Overall, the symmetric component of the wind anomalies at a given time is consistent with the classical Gill (1980) response to heating on the equator, consisting of a KW packet to the east of the heating and two RW packets to the west. The latter correspond at upper levels to a pair of anticyclonic (cyclonic) RW gyres that are symmetric with respect to the equator and trail the positive (negative) heating anomalies.

Recently, Drbohlav and Wang (2005) used an axially symmetric model to examine the mechanism of northward propagation. They show that the northward propagation in the model is produced by the free-troposphere barotropic divergence, which leads convection by about a quarter of a cycle. The vertical advection of summer mean easterly vertical wind shear by perturbation vertical motion inside the convective region induces barotropic divergence (convergence) to the north (south) of convection. This barotropic divergence triggers moisture convergence in the boundary layer to the north of convection, causing the northward propagation of precipitation. Another possible mechanism for northward propagation is what it develops as a result of surface frictional convergence within the RW response (highlighted by Lawrence and Webster 2002). A third possibility is that the off-equatorial precipitation develops as a result of wind–evaporation feedback (Maloney and Esbensen 2005).

We examine the above mechanisms in Fig. 7, which shows the northward propagation of the precipitation anomaly around 80°–85°E during the MJO cycle together with surface divergence, barotropic divergence, and evaporation. The barotropic divergence is computed as a mean of the divergence at 200 and 850 hPa following Drbohlav and Wang (2005). The figure shows that only surface frictional convergence leads the northward propagation of the positive precipitation anomalies (neither barotropic divergence nor surface evaporation). This suggests that the most likely mechanism responsible for the northward propagation is surface frictional convergence, as suggested by Lawrence and Webster.

c. Boreal winter (November–April)

We next focus on boreal winter (Figs. 8 and 9). Here we are primarily interested in the links between the MJO and the Australian summer monsoon, so we pick a base region index that is farther to the east (4°–4°N, 90°–120°E). Figure 8 shows the observed and simulated precipitation, surface wind, and 200-hPa streamfunction composites. The spatial patterns of the eastward-moving anomalies are reasonably well simulated. The main discrepancies with the observations are largely the same as those of the boreal summer season: the anomalies are roughly a factor 2 too large, especially over Indonesia and the Pacific warm pool.

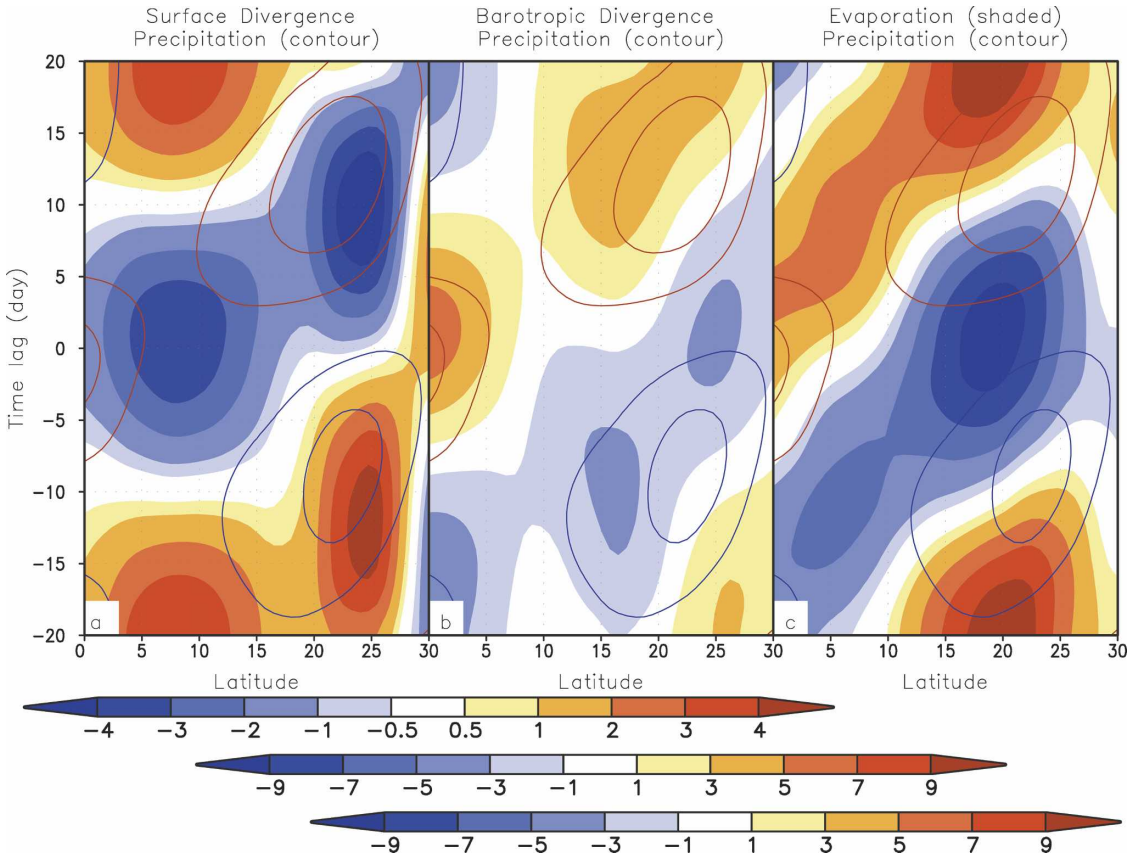

FIG. 7. Latitude–time cross section of (a) precipitation (mm day^{-1}, contour at every 0.5 mm day^{-1}; red is for positive anomalies and blue for negative anomalies) and surface frictional divergence (10^{-6} s^{-1}, shaded), (b) precipitation (contour) and barotropic divergence (shaded), and (c) precipitation (contour) and evaporation (W m^{-2}, shaded).

The boreal winter precipitation anomalies show much more of an equatorial east–west dipole structure and symmetry with respect to the equator compared with boreal summer (cf. Fig. 6). Beginning at −10 days, we see that negative anomalies extend over much of the Tropics from the eastern Indian Ocean into Indonesia, while positive anomalies are beginning to develop in the western Indian Ocean in association with easterly surface wind anomalies. At −5 days there is a split in the negative anomalies over Indonesia in association with cyclonic wind anomalies in both hemispheres. The negative anomalies in the Southern Hemisphere extend southward, acting to reduce precipitation over northern Australia through day 0. The off-equatorial negative anomalies do not develop further and by day 5 have largely been replaced by the large equatorial positive anomaly that propagates into the western Pacific.

At day 10 the precipitation maximum has split so that east–west bands of precipitation stretch across the Indian Ocean on either side of the equator (Fig. 8). In the Southern Hemisphere, the positive anomalies extend sufficiently far eastward to enhance precipitation over northern Australia. The observations show a clear asymmetry with respect to the equator at this time, with larger (smaller) anomalies occurring in the Southern (Northern) Hemisphere. The larger summer hemisphere anomalies develop in association with northwesterly surface wind anomalies emanating from the developing negative equatorial precipitation anomaly, reminiscent of the Northern Hemisphere summer results discussed earlier. Similar asymmetries also occur between the hemispheres somewhat earlier (days 0 and 5) in both observations and simulation though, overall, both the observations and simulations show much greater symmetry with respect to the equator than was the case for the boreal summer. These differences between the two seasons are explored further in the next section.

The composite upper-level streamfunction at 200 hPa for the observations and the model simulations (Fig. 8) are quite similar though, as was the case for the boreal summer, the amplitude is roughly a factor of 4 larger in the simulation. The main features again consist of an eastward propagating quadrapole pattern of stream-

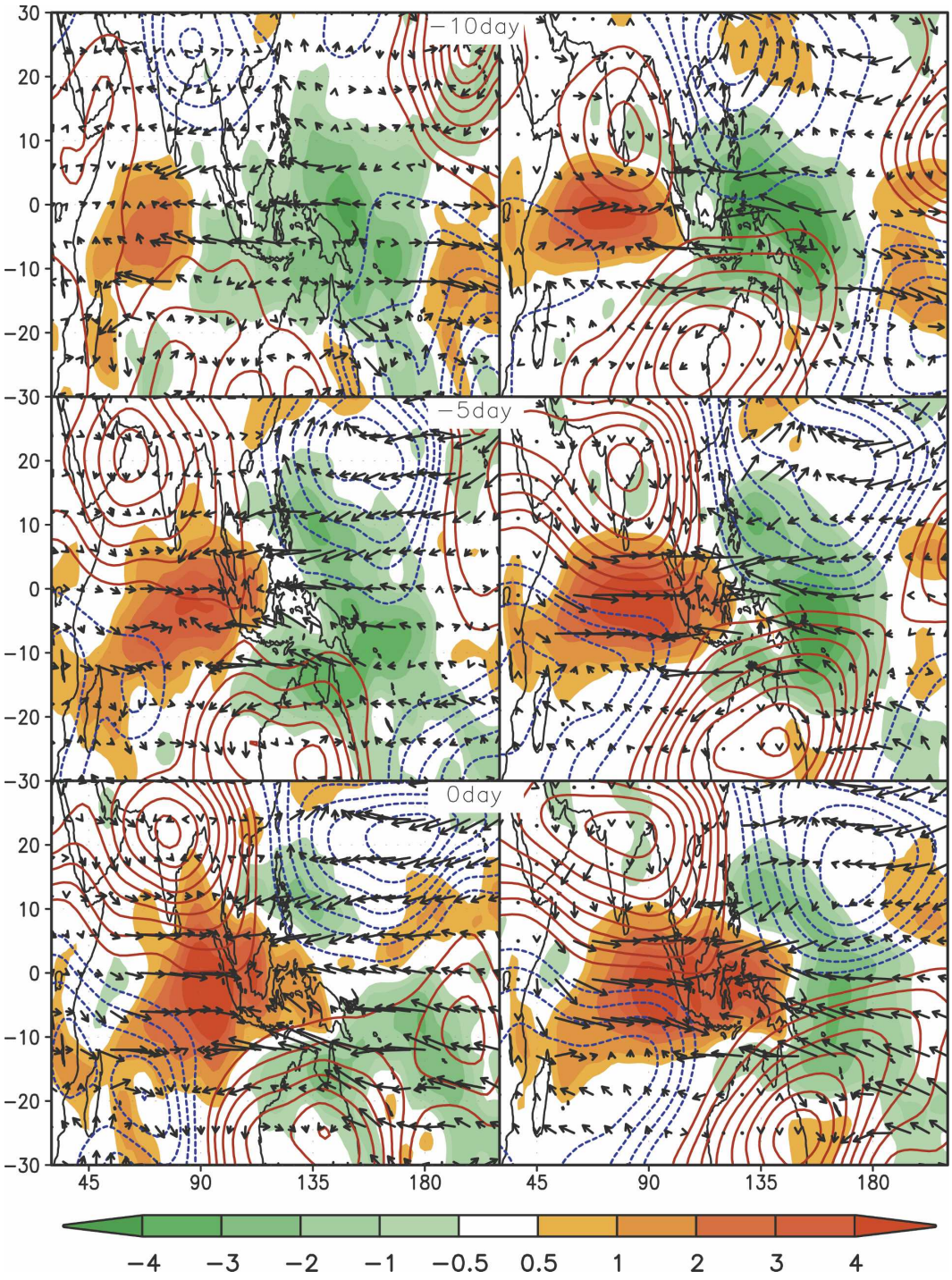

FIG. 8. As in Fig. 6, but for November–April.

function anomalies, though in this case they are most evident somewhat lower in the troposphere (about 200 mb) compared with boreal summer. The anomalies span the region from Africa to well west of the date line. For example at day −15, two anticyclonic anomalies straddle the equator over the eastern equatorial Pacific, while cyclonic anomalies occur to the west. The associated easterlies to the east and westerlies to the west are consistent with upper-level convergence over the western Pacific and suppressed precipitation (see

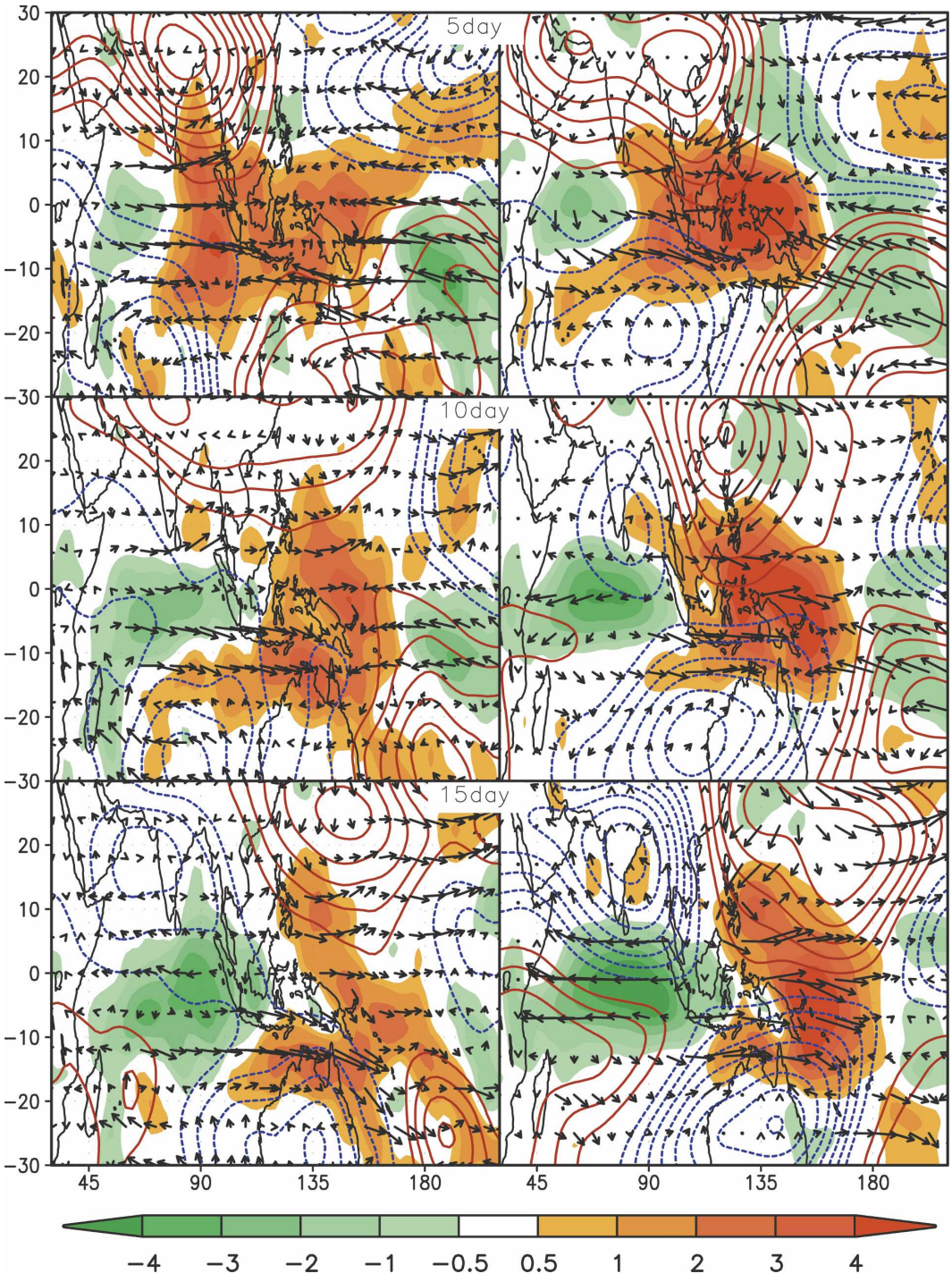

FIG. 8. (*Continued*)

Fig. 8). At day 0, the pattern has propagated far enough to the east so that the anomalies have changed sign and the region is apparently now dominated by large-scale divergence. The basic structure of the wind, streamfunction, and precipitation is again generally consistent with the Gill model response to equatorial heating, with a KW packet to the east and RW gyres to the west of the heating.

As in the summer case, the upper-level streamfunction in Fig. 8 shows that both observations and simula-

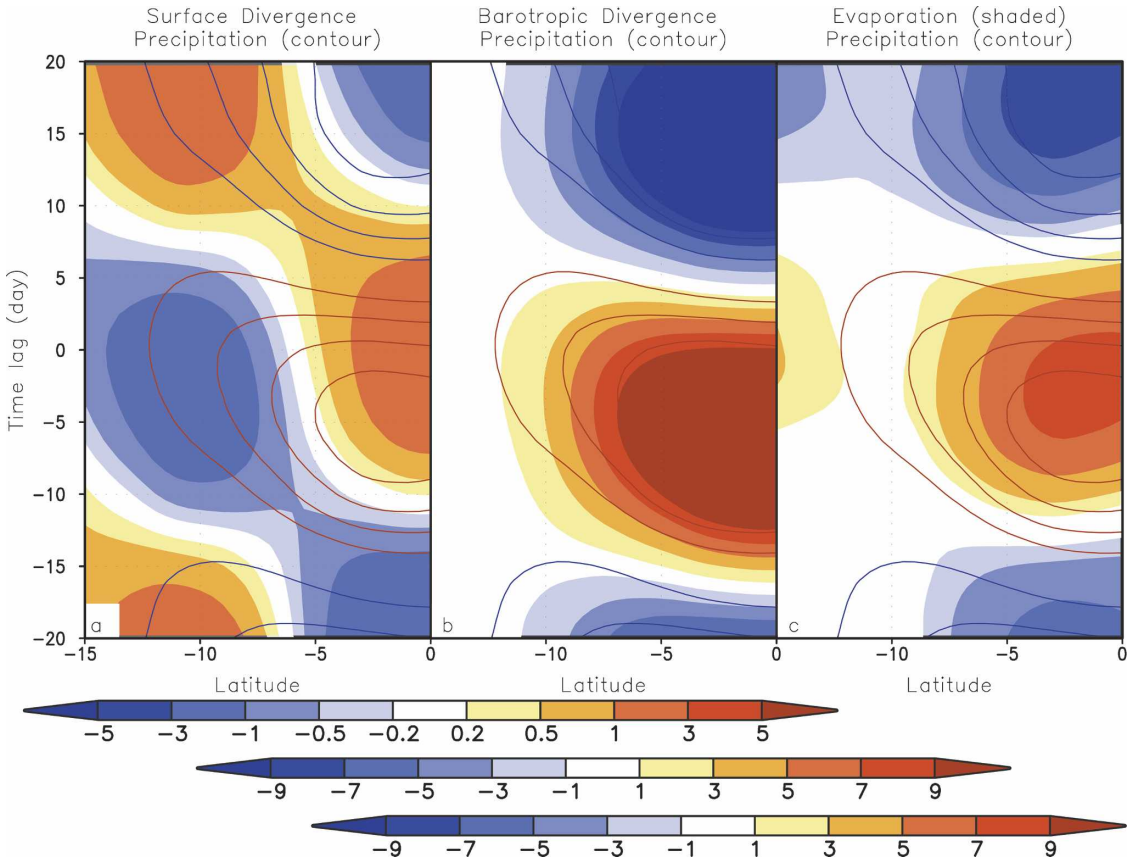

FIG. 9. As in Fig. 7, but for November–April.

tions have a quadrapole structure with a coherent eastward movement tied to the precipitation/heating anomalies. The structure is again coherent, with westerly wind anomalies just to the east of the heating and easterlies to the east.

Looking at the nature of the southward propagation of the precipitation, we again plot (Fig. 9) the precipitation anomalies together with surface divergence, barotropic divergence, and evaporation. Similar to the boreal summer case, we see that only the surface frictional convergence leads the southward propagation of the positive precipitation anomalies, suggesting that the mechanism proposed by Lawrence and Webster (2002) is also operating during boreal winter.

We now turn our attention to the causes of the hemispheric asymmetries in the off-equatorial precipitation anomalies.

4. Seasonal changes in the base state

Since the prescribed heating does not vary by season, the above results support the idea (Wang and Xie 1997) that the seasonal differences in the off-equatorial precipitation and surface winds are primarily driven by the seasonal changes in the basic state (e.g., including vertical wind shear, low-level moisture distribution).

We begin by looking at the seasonal changes in the vertical shear of the zonal wind (Fig. 10). Xie and Wang (1996) and Wang and Xie (1996, 1997) show that easterly shear favors emanation of Rossby waves. They discussed that the tropical Rossby wave have two energy sources: one is vertical shear of the mean zonal flow via baroclinic instability and the other is the surface friction-induced moist convergence. Both processes contribute to the development of the tropical Rossby wave. In the presence of the boundary layer, the moist Rossby wave instability is remarkably enhanced by easterly vertical shears. This results form the fact that an easterly shear confines the wave to the lower level, generating a stronger Ekman-pumping-induced heating. When the shear is asymmetric relative to the equator, the unstable Rossby wave is constrained to the hemisphere where the shear is prominent. This helps in the explanation of the emanation of equatorial waves toward midlatitudes. The northwestward emanation of Rossby waves were observed and documented by

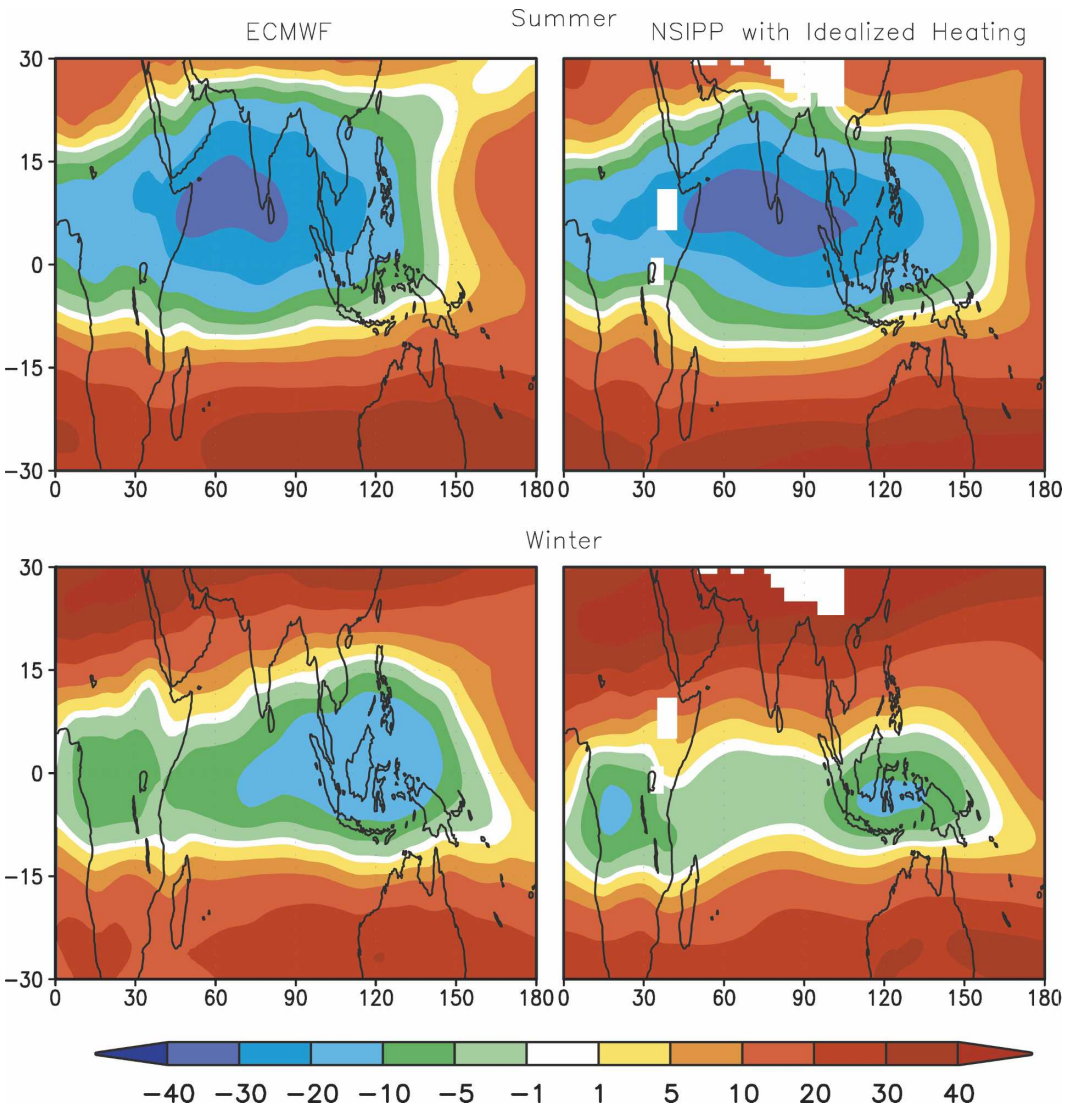

FIG. 10. Summer and winter vertical shear (200–850 mb) of the wind (m s^{-1}): (top) ECMWF 40-year Re-Analyses, and (bottom) model simulations.

Kemball-Cook and Wang (2001) and Lawrence and Webster (2002).

In Figure 10 both the observations (reanalysis) and the model simulations show a strong asymmetry with respect to the equator in the region of easterly shear during boreal summer. The easterly shear occurs primarily in the Northern Hemisphere extending from about 5°S latitude to about 25°N latitude and covers much of the South Asian monsoon region. The largest shear occurs at about 10°N and extends from the east coast of Africa across the southern tip of India. In the simulations, the region of high shear extends still farther east to Indo–China. In contrast, during boreal winter the observations show that the region of easterly shear is largely symmetric with respect to the equator, with the region of largest shear centered over Indonesia. The model results, however, show greater asymmetry with respect to the equator with substantially less easterly shear north of the equator. Overall, the easterly shear during boreal winter is weaker and latitudinally more confined compared with that of boreal summer.

We next consider that changes in the thermodynamic structure of the base state can influence the occurrence of precipitation. To do this we examine the convective available potential energy, defined as

$$R_d\text{CAPE} = R_d \int_{pn}^{pi} (T_{vp} - T_v)\, d\ln p, \qquad (1)$$

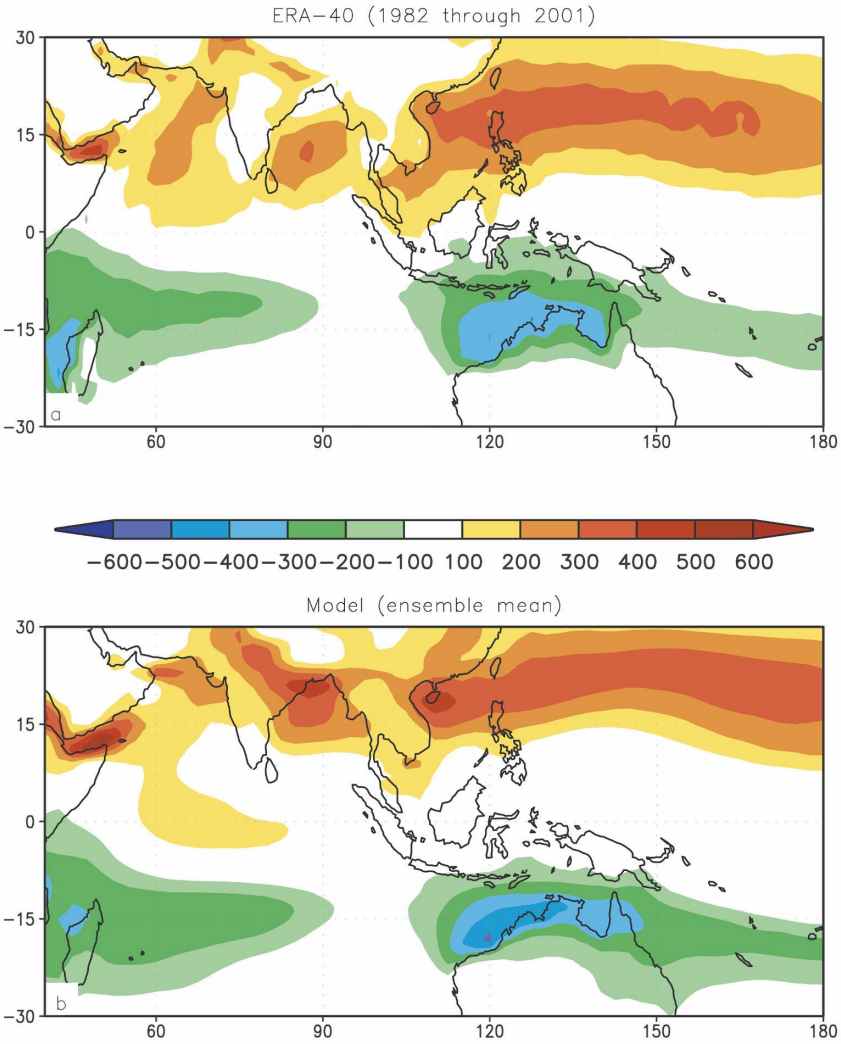

FIG. 11. As in Fig. 10, but for the convective available potential energy (J kg^{-1}).

where R_d is the gas constant, T_{vp} and T_v are the virtual temperature of parcel and environment, respectively, and p_n and p_i are cloud-top pressure and pressure to which the parcel lifted, respectively. This is a vertical integral of buoyancy of a lifted parcel and can be interpreted as the maximum available energy that can be transferred to the deep convective motion.

The seasonal mean differences (boreal summer minus boreal winter) in the observed and simulated CAPE (Fig. 11) show the expected larger CAPE in the summer hemispheres. In the Northern Hemisphere, the differences are largest over the eastern Pacific north of about 15° and over the Arabian Sea and Bay of Bengal. In the Southern Hemisphere, the differences are largest near 15°S in the eastern Indian Ocean and just north of Australia. The above results suggest that both the shear (through its affect on the Rossby wave response) and CAPE favor an off-equatorial response in the Northern Hemisphere during boreal summer.

5. Conclusions

Considerable progress has been made in understanding the basic mechanism of the MJO. Nevertheless, the pronounced seasonality of the MJO is still poorly understood. In this study, observations and AGCM (NSIPP-1) simulations were used to further address a key aspect of that seasonality, namely, the apparent meridional propagation that appears to be a major factor in how the MJO influences the Asian and Australian summer monsoons.

The NSIPP-1 model, like many other AGCMs, pro-

duces only a weak MJO. Here, we take advantage of that model's shortcoming to isolate the model response to an imposed equatorial (MJO like) heating.

A key result of this study is that the AGCM, when forced with idealized eastward propagating equatorial dipole heating anomalies, reproduces the salient features of the observed MJO seasonality. This includes the greater east–west orientation and symmetry with respect to the equator of the precipitation anomalies during boreal winter and the tendency for the anomalies to have a more north–south structure during boreal summer. The simulations also show clear evidence of apparent meridional propagation and the associated impacts on the Asian and Australian summer monsoons, which are similar to those observed. Since the prescribed heating has no seasonality, these features of the MJO are driven by the seasonal changes in the basic state.

An analysis of the model simulations shows that the response to the prescribed heating consists of surface easterlies to the east of the heating center and westerlies over and to the west of the heating center, while an anticyclone pair develops on either side of the equator. The basic structure of the wind is consistent with the classical Gill response to heating on the equator consisting of a KW packet to the east of the heating and two Rossby wave cells to the west of and over the heating.

Further analysis shows that the initial development of the off-equatorial response to the leading pole of the equatorial heating is the result of frictional convergence within the Rossby wave response, consistent with the findings of Lawrence and Webster (2002). Further development of the off-equatorial response, however, appears to depend crucially on the east–west dipole nature of the equatorial heating. In particular, it is the interaction of the nascent off-equatorial precipitation and wind anomalies with the trailing pole of the equatorial dipole that acts to enhance and extend the anomalies to produce the characteristic northwest to southeast (or southwest to northeast) tilt of the off-equatorial precipitation anomalies.

An analysis of the seasonal changes in the background state suggest that changes in both the static stability (CAPE) and the vertical wind shear favor the development of off-equatorial precipitation anomalies in the Northern Hemisphere during boreal summer, consistent with Wang and Xie (1997). During boreal winter, there is some tendency to favor off-equatorial development in the Southern Hemisphere, though less so.

To summarize, Fig. 12 presents a schematic of the development of the precipitation and surface wind anomalies during boreal summer. The first panel shows the initial split of the equatorial positive precipitation anomaly associated with the surface cyclones of the Rossby wave response. The remnants of the previous negative precipitation anomaly (together with northeasterly wind anomalies) are situated to the northeast. During the next stage (second panel), only the Northern Hemisphere cyclonic anomaly survives. Southwesterlies develop in association with the developing trailing negative pole of the equatorial precipitation dipole. The southwesterlies, together with the surface cyclone, produce a line of convergence and enhanced precipitation anomalies that eventually extend in a northwest to southeast direction across the Arabian Sea, India, and the Bay of Bengal (third panel). If we include the remnants of the eastward propagating positive pole of the equatorial anomaly, the line extends well into Indonesia. The subsequent development for the negative

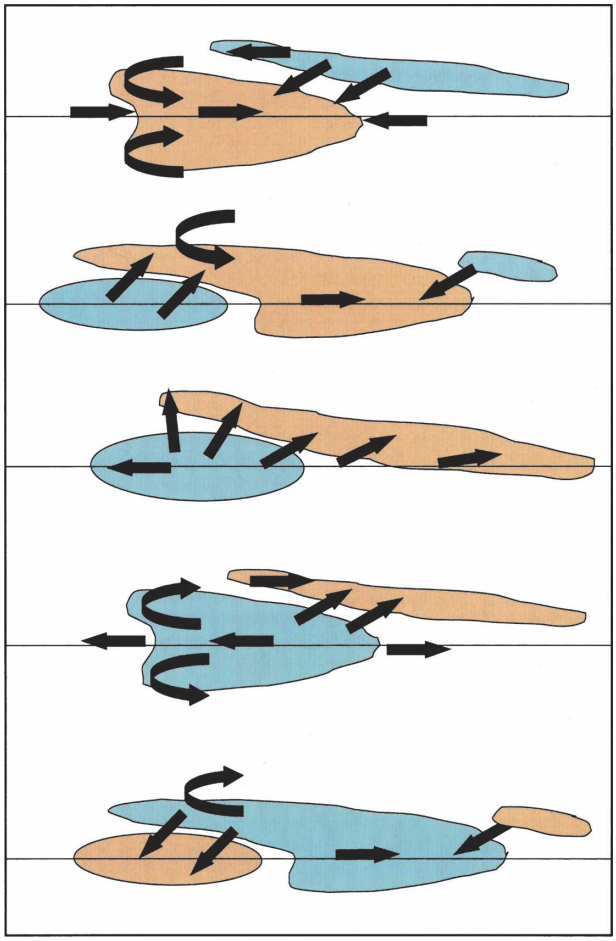

FIG. 12. A schematic depiction of the precipitation and low-level wind anomalies associated with the MJO over the Asian summer monsoon region.

anomalies is analogous (see, e.g., the fourth and fifth panels).

Acknowledgments. This work was supported by the NASA Science Mission Directorate's Modeling and Analysis Program. D. Waliser was supported by the Human Resource's Development Fund at the Jet Propulsion Laboratory (JPL), as well as the National Science Foundation (Grant ATM-0094416). The research performed at JPL, California Institute of Technology, was performed under contracts with the National Aeronautics and Space Administration.

REFERENCES

Annamalai, H., and J. M. Slingo, 2001: Active/break cycles: Diagnosis of the intraseasonal variability of the Asian summer monsoon. *Climate Dyn.,* **18,** 85–102.

——, ——, K. R. Sperber, and K. Hodges, 1999: The mean evolution and variability of the Asian summer monsoon: Comparison of ECMWF and NCEP–NCAR reanalyses. *Mon. Wea. Rev.,* **127,** 1157–1186.

Arakawa, A., and M. J. Schubert, 1972: Interaction of a cumulus cloud ensemble with the large-scale environment, Part I. *J. Atmos. Sci.,* **31,** 671–701.

——, and M. J. Suarez, 1983: Vertical differencing of the primitive equations in sigma coordinates. *Mon. Wea. Rev.,* **111,** 34–45.

Atlas, R., R. N. Hoffman, S. C. Bloom, J. C. Jusem, and J. Ardizzone, 1996: A multiyear global surface wind velocity dataset using SSM/I wind observations. *Bull. Amer. Meteor. Soc.,* **77,** 869–882.

——, and Coauthors, 2001: The effect of marine winds from scatterometer data on weather analysis and forecasting. *Bull. Amer. Meteor. Soc.,* **82,** 1965–1990.

Bacmeister, J. T., and M. J. Suarez, 2002: Wind stress simulations and equatorial dynamics in an AGCM. *J. Atmos. Sci.,* **59,** 3051–3073.

——, P. J. Pegion, S. D. Schubert, and M. J. Suarez, 2000: *An Atlas of Seasonal Means Simulated by the NSIPP 1 Atmospheric GCM*. NASA Tech. Memo. 104606, Vol. 17, 194 pp.

Chen, T.-C., and M. Murakami, 1988: The 30–50 day variation of convective activity over the western Pacific Ocean with the emphasis on the northwestern region. *Mon. Wea. Rev.,* **116,** 892–906.

Chou, M.-D., and M. J. Suarez, 1994: An efficient thermal infrared radiation parameterization for use in general circulation models. NASA Tech. Memo. 104606, Vol. 3, 85 pp.

——, and ——, 1999: A solar radiation parameterization for atmospheric studies. NASA Tech. Memo. 104606, Vol. 11, 40 pp.

Drbohlav, H.-K. L., and B. Wang, 2005: Mechanism of the northward-propagating intraseasonal oscillation: Insights from a zonally symmetric model. *J. Climate,* **18,** 952–972.

Ferranti, L., J. M. Slingo, T. N. Palmer, and B. J. Hoskins, 1999: The effect of land surface feedbacks on the monsoon circulation. *Quart. J. Roy. Meteor. Soc.,* **125,** 1527–1550.

Gadgil, S., 1990: Poleward propagation of the ITCZ: Observations and theory. *Mausam,* **41,** 285–290.

Gibson, J. K., P. Kallbert, and S. Uppala, 1996: The ECMWF ReAnalysis (ERA) Project. *ECMWF Newsletter,* No. 73, 7–17.

Gill, A. E., 1980: Some simple solutions for heat-induced tropical circulation. *Quart. J. Roy. Meteor. Soc.,* **106,** 447–462.

Hendon, H. H., and J. L. Salby, 1994: The life cycle of the Madden–Julian oscillation. *J. Atmos. Sci.,* **51,** 2207–2219.

Kemball-Cook, S. R., and B. Wang, 2001: Equatorial waves and air–sea interaction in the boreal summer intraseasonal oscillation. *J. Climate,* **14,** 2923–2942.

Kiladis, G. N., and K. M. Weickmann, 1992: Circulation anomalies associated with tropical convection during northern winter. *Mon. Wea. Rev.,* **120,** 1900–1923.

Krishnamurti, T. N., and D. Subrahmanyam, 1982: The 30–50 day mode at 850 mb during MONEX. *J. Atmos. Sci.,* **39,** 2088–2095.

Lau, K.-M., and P. H. Chan, 1986: Aspects of the 40–50 day oscillation during the northern summer as inferred from outgoing long-wave radiation. *Mon. Wea. Rev.,* **114,** 1354–1367.

——, and P. L. Peng, 1990: Origin of low frequency (intraseasonal) oscillations in the tropical atmosphere. Part III: Monsoon dynamics. *J. Atmos. Sci.,* **47,** 1443–1462.

Lawrence, D. M., and P. J. Webster, 2002: The boreal summer intraseasonal oscillation: Relationship between northward and eastward movement of convection. *J. Atmos. Sci.,* **59,** 1593–1605.

Louis, J., M. Tiedtke, and J. Geleyn, 1982: A short history of the PBL parameterization at ECMWF. *Proc. ECMWF Workshop on Planetary Boundary Layer Parameterization,* Reading, United Kingdom, ECMWF, 59–80.

Madden, R. A., and P. R. Julian, 1972: Description of global-scale circulation cells in the tropics with a 40–50 day period. *J. Atmos. Sci.,* **29,** 1109–1123.

Maloney, E. D., and D. L. Hartmann, 1998: Frictional moisture convergence in a composite life cycle of the Madden-Julian oscillation. *J. Climate,* **11,** 2387–2403.

——, and S. K. Esbensen, 2005: A modeling study of summertime east Pacific wind-induced ocean–atmosphere exchange in the intraseasonal oscillation. *J. Climate,* **18,** 568–584.

McBride, J. L., 1983: Satellite observations of the southern hemisphere monsoon during Winter MONEX. *Tellus,* **35,** 189–197.

Moorthi, S., and M. J. Suarez, 1992: Relaxed Arakawa-Schubert: A parameterization of moist convection for general circulation models. *Mon. Wea. Rev.,* **120,** 978–1002.

Oppenheim, A. V., and R. W. Schafer, 1975: *Digital Signal Processing*. Prentice-Hall, 585 pp.

Park, C.-K., M. J. Suarez, and S. D. Schubert, 1995: Response of the zonally asymmetric flow to time-dependent tropical heating. *J. Atmos. Sci.,* **52,** 3738–3756.

Pegion, P. J., S. D. Schubert, and M. J. Suarez, 2000: An assessment of the predictability of northern winter seasonal means with the NSIPP 1 AGCM. NASA Tech. Memo. 104606, Vol. 18, 110 pp.

Radok, U., 1971: The Australian region and the general circulation of the southern hemisphere. *Climates of Australia and New Zealand*, J. Gentilli, Ed., *World Survey of Climatology,* Vol. 13, Elsevier, 13–33.

——, and A. M. Grant, 1957: Variations in the high tropospheric mean flow over Australia and New Zealand. *J. Meteor.,* **14,** 141–149.

Rayner, N. A., D. E. Parker, E. B. Horton, C. K. Folland, L. V. Alexander, D. P. Rowell, E. C. Kent, and A. Kaplan, 2003: Global analyses of sea surface temperature, sea ice, and night marine air temperature since the late nineteenth century. *J. Geophys. Res.,* **108,** 4407, doi:10.1029/2002JD002670.

Sardshmukh, P. D., and B. J. Hoskins, 1988: The generation of

global rotational flow by steady idealized tropical divergence. *J. Atmos. Sci.,* **45,** 261–278.

Schubert, S. D., M. J. Suarez, P. J. Pegion, M. A. Kistler, and A. Kumer, 2002: Predictability of zonal means during boreal summer. *J. Climate,* **15,** 420–434.

Suarez, M. J., and L. L. Takacs, 1995: Documentation of the Aries-GEOS dynamical core: Version 2. NASA Goddard Space Flight Center, Tech. Memo. 104606, Vol. 5, 45 pp.

Waliser, D., S. Schubert, A. Kumar, K. Weickman, and R. Dole, 2003: Proceedings from a workshop on "Modeling, Simulation and Forecasting of Subseasonal Variability." NASA/CP 2003-104606, Vol. 25, 62 pp.

Wang, B., and H. Rui, 1990: Synoptic climatology of transient tropical intraseasonal convection anomalies: 1975–1985. *Meteor. Atmos. Phys.,* **44,** 43–61.

——, and X. Xie, 1996: Low-frequency equatorial waves in vertically sheared zonal flow. Part I: Stable waves. *J. Atmos. Sci.,* **53,** 449–467.

——, and ——, 1997: A model for the boreal summer intraseasonal oscillation. *J. Atmos. Sci.,* **54,** 72–86.

Webster, P. J., 1972: Response of the tropical atmosphere to local, steady forcing. *Mon. Wea. Rev.,* **100,** 518–541.

Wu, M.-L., S. Schubert, and N. E. Huang, 1999: The development of the South Asian summer monsoon and the intraseasonal oscillation. *J. Climate,* **12,** 2054–2075.

Xie, P., and P. A. Arkin, 1997: Global precipitation: A 17-year monthly analysis based on gauge observations, satellite estimate, and numerical model outputs. *Bull. Amer. Meteor. Soc.,* **78,** 2539–2558.

Xie, X., and B. Wang, 1996: Low-frequency equatorial waves in vertically sheared zonal flow. Part II: Unstable waves. *J. Atmos. Sci.,* **53,** 3589–3605.

Yasunari, T., 1981: Structure of an Indian summer monsoon system with a period around 40 days. *J. Meteor. Soc. Japan,* **59,** 336–354.